Crack Detection in a Rotor Dynamic System by Vibration Monitoring—Part II: Extended Analysis and Experimental Results

Philip Varney[1]
Graduate Research Assistant
e-mail: pvarney3@gatech.edu

Itzhak Green
Professor
e-mail: itzhak.green@me.gatech.edu

Woodruff School of Mechanical Engineering,
Georgia Institute of Technology,
Atlanta, GA, 30332

An increase in the power-to-weight ratio demand on rotordynamic systems causes increased susceptibility to transverse fatigue cracking of the shaft. The ability to detect cracks at an early stage of progression is imperative for minimizing off-line repair time and cost. The vibration monitoring system initially proposed in Part I is employed herein, using the 2X harmonic response component of the rotor tilt as a signature indicating a transverse shaft crack. In addition, the analytic work presented in Part I is expanded to include a new notch crack model to better approximate experimental results. To effectively capture the 2X response, the crack model must include the local nature of the crack, the depth of the crack, and the stiffness asymmetry inducing the gravity-forced 2X harmonic response. The transfer matrix technique is well suited to incorporate these crack attributes due to its modular nature. Two transfer matrix models are proposed to predict the 2X harmonic response. The first model applies local crack flexibility coefficients determined using the strain energy release rate, while the second incorporates the crack as a rectangular notch to emulate a manufactured crack used in the experiments. Analytic results are compared to experimental measurement of the rotor tilt gleaned from an overhung rotor test rig originally designed to monitor seal face dynamics. The test rig is discussed, and experimental angular response orbits and 2X harmonic amplitudes of the rotor tilt are provided for shafts containing manufactured cracks of depths between 0% and 40%. Feasibility of simultaneous multiple-fault detection of transverse shaft cracks and seal face contact is discussed. [DOI: 10.1115/1.4007275]

1 Introduction

The demand placed on modern rotating machinery results in high operating stresses, which increases susceptibility to transverse cross-section fatigue cracking of the shaft. The capability to detect these cracks at an early stage of progression is imperative not only for safety but also for economy. Early shaft crack detection allows the operator to plan accordingly for repair, without the need to prematurely take the system off-line for an extended period of time.

The first step in development of an online crack detection system is the identification of unique system response characteristics induced by a shaft crack. Numerous crack models have been developed that attribute the appearance of a 2X shaft speed harmonic to the presence of a transverse shaft crack [1–10]. The 2X harmonic, appearing at a frequency equal to twice the shaft speed and reaching resonance at a shaft speed equal to half of a natural frequency, arises due to stiffness asymmetry in the system in the presence of a fixed or stationary forcing such as gravity [1,2]. For this reason, shafts with dissimilar area moments of inertia also display a prominent 2X harmonic [1–3,6,8,9].

The extent to which a globally asymmetric shaft model can be used to approximate a system with a highly localized shaft crack is limited. It is well known [5–7] that the position of the crack along the shaft greatly influences the magnitude of the 2X harmonic response. Any reasonable model of a cracked shaft must account for this localization.

Cracks can be categorized into gaping (open) cracks [1,3,6,10,11] and breathing cracks [3–10]. Gaping cracks remain open regardless of the angle of rotation of the shaft. This assumption is generally valid in systems with small static displacements and vibrational amplitudes [6,9]. As such, it is reasonable to assume that the dominant characteristic of a gaping crack is the localized reduction in stiffness.

In Part I, Casey and Green [1] employ two models to approximate the characteristics of a gaping crack. The first model uses the depth of the crack to create a system displaying global shaft asymmetry; the global nature of the asymmetry allows for an analytical steady-state solution of the system equations of motion. Four degrees of freedom are used: two displacements and two tilts. A gravity-forced response analysis indicates that the 2X harmonic resonant magnitude increases as crack depth (or level of asymmetry) increases, while the frequency at which the 2X harmonic resonance occurs decreases.

The next model approximates the localization of the crack via crack flexibility coefficients, as per the strain energy release rate (SERR) [1,3,4,9–13]. The additional flexibilities caused by the crack are incorporated into a transfer matrix allowing for the localization of the crack along the shaft. The extended transfer matrix, as provided by Lee and Green [14] and originally proposed by Pestel and Leckie [15], allows for expansion of the transfer matrix to include forcing. As crack depth increases, the gravity-forced response of the system predicts a decrease in the 2X resonant frequency with an increase in magnitude, though

[1]Corresponding author.

Manuscript received May 16, 2012; final manuscript received July 28, 2012; published online September 20, 2012. Assoc. Editor: Jaroslaw Szwedowicz.

the decrease in frequency is less pronounced when compared to the globally asymmetric shaft model.

Contrary to gaping cracks, breathing cracks open and close periodically as a function of the shaft's angle of rotation, causing the stiffness to vary as a function of rotation angle. The impact and rubbing induced by the opening and closing motion of the breathing crack gives rise to increased damping caused by frictional dissipation [4]. The aforementioned characteristics of a breathing crack are responsible for the appearance of additional harmonics occurring at integer multiples of the shaft speed [4–8]. A myriad of models employing time-dependent stiffness coefficients are available to describe breathing cracks: various nonlinear equations of motion [8], an adapted SERR approach [4], and stepped stiffness functions [12,16,17].

The ability of a model to emulate the actual nature of the crack is imperative for quantitatively predicting the response. Careful consideration must be given to deduce which crack model best suits the system. In this work, an experimental procedure for crack detection using an existing vibration monitoring system is discussed. The vibration monitoring system was originally constructed to monitor flexibly mounted rotor (FMR) mechanical face seal dynamics [14,18–20]. The ability of the test rig to detect higher harmonics due to seal face contact is discussed in Ref. [20], and an active control system is proposed by Dayan, Zou, and Green [21] to eliminate the contact. Modifications to the test rig allowing shaft crack detection, as first proposed in Part I, are provided herein with the goal of discussing the feasibility of simultaneous multiple-fault detection.

The experimental and analytic results of two gaping crack models are compared. The first model incorporates local crack flexibility coefficients derived from the SERR, while the second approximates the manufactured crack as a small rectangular notch. Plots of the 2X harmonic tilt response versus shaft speed are provided for several crack depths, as well as experimentally measured angular response orbits.

2 Forced Response: Local Crack Flexibility Model

An appropriate crack model must account for the additional compliance caused by the crack. One widely used method employs the SERR along with linear elastic fracture mechanics theory to estimate the additional compliance caused by the crack [3,13]. The method was first proposed by Irwin [22] and subsequently extended to rotordynamic systems of six degrees of freedom by Dimarogonas and Paipetis [13]. The additional displacement u_i, along the direction of force P_i, caused by a transverse crack of depth a is

$$u_i = \frac{\partial}{\partial P_i}\int_0^a J(y)dy \tag{1}$$

where $J(y)$ is the SERR [4] and y denotes the direction parallel to the crack depth, as shown in Fig. 1. The xy frame shown in the figure is a shaft-fixed reference frame that rotates with the shaft and always maintains its orientation relative to the crack edge. The uncracked section of the circular shaft of radius R is represented by hatching, and the half-width of the crack is b.

The SERR $J(y)$ depends on several factors: the elastic modulus and the Poisson ratio of the shaft material, the stress intensity factors (SIF) corresponding to the geometry of the cracked section, and the applied loads. The SIFs are provided by Papadopoulos and Dimarogonas [3] for a circular cross section containing a transverse crack. The additional compliance c_{ij} caused by the crack is a flexibility in the i^{th} direction caused by application of a force in the j^{th} direction, and is found by integrating the definition of displacement, Eq. (1), along the length of the crack edge:

$$c_{ij} = \frac{\partial u_i}{\partial P_j} = \frac{\partial^2}{\partial P_i \partial P_j}\int_{-b}^{b}\int_0^a J(y)dydx \tag{2}$$

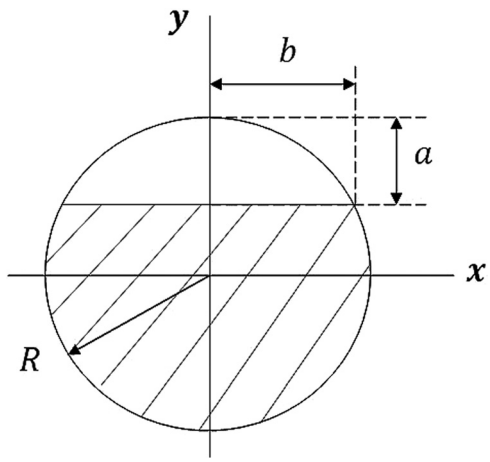

Fig. 1 Cross section of shaft containing transverse crack

The dimension of the crack compliance matrix is reduced from six to four, as axial and torsional deflection are neglected. The crack compliances of interest relate the shear force V and bending moment M to the linear and angular displacements u and θ (in directions x and y) according to

$$\begin{Bmatrix} u_x \\ u_y \\ \theta_y \\ \theta_x \end{Bmatrix} = \begin{bmatrix} c_{22} & 0 & 0 & 0 \\ 0 & c_{33} & 0 & 0 \\ 0 & 0 & c_{44} & c_{45} \\ 0 & 0 & c_{54} & c_{55} \end{bmatrix} \begin{Bmatrix} V_x \\ V_y \\ M_y \\ M_x \end{Bmatrix} \tag{3}$$

where $c_{45} = c_{54}$. The compliance matrix shown above can easily be rearranged into a transfer matrix, as demonstrated by Casey and Green in Part I [1]. The crack transfer matrix updates the state vector $\{S\}$ from the left side of the crack to the right side according to

$$\{S\}^{\text{Right}} = [F_{\text{crack}}]\{S\}^{Left} \tag{4}$$

where $[F_{\text{crack}}]$ is the crack transfer matrix provided in Part I [1], and summarized in Appendix A. The state vector $\{S\}$ is

$$\{S\} = \{u_x\ \theta_y\ M_y - V_x - u_y\ \theta_x\ M_x\ V_y\}^T \tag{5}$$

where the direction of the state vector quantity is indicated by the subscript. A more comprehensive treatise on the state vector terms can be found in Ref. [14].

An overhung rotordynamic system of shaft speed n and length L is shown in Fig. 2, with a crack located a distance L_1 from the clamped support. The remaining distance to the rotor is designated L_2, and the width of the crack is assumed to be negligible. The shaft-fixed xyz frame shown in the figure is equivalent to that shown in Fig. 1.

It is well known that forcing due to gravity gives rise to the 2X harmonic response. The transfer matrix was adapted to include

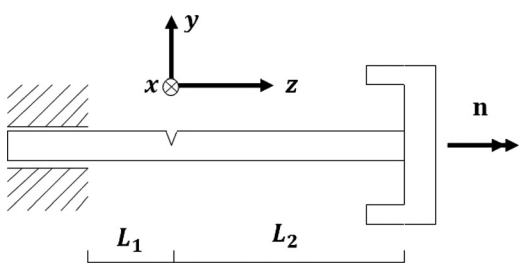

Fig. 2 Overhung rotor system with transverse shaft crack

forcing by Lee and Green [14] and described in detail by Casey and Green in Part I [1] for a cracked system. In order to incorporate forcing due to gravity, the transfer matrix must be expanded from 8×8 to 9×9, and an additional entry of unity is concatenated onto the end of the state vector:

$$\{S\} = \{u_x\ \theta_y\ M_y\ -V_x\ -u_y\ \theta_x\ M_x\ V_y 1\}^T \tag{6}$$

The field matrices and point matrices for a rotating reference frame transfer matrix analysis, incorporating forcing due to gravity, are provided and discussed in Part I [1]. The field matrices to the left and right of the crack are designated $[F_1]$ and $[F_2]$, respectively, while the point matrix corresponding to the lumped inertia of the rotor and damping effects is designated $[P]$. Note that the inertia of the shaft is neglected in comparison to that of the rotor. For convenience, $[P]$ and $[F]$ are summarized in Appendix A. The total transfer matrix $[U]$ is found via successive multiplication of element transfer matrices:

$$[U] = [P][F_2][F_{\text{crack}}][F_1] \tag{7}$$

where $[U]$ is size 9×9. The overall transfer matrix in Eq. (7) updates the state vector from the left support to the right support. As such, application of clamped-free boundary conditions results in expressions used to obtain the forced response of the system:

$$\begin{bmatrix} U_{33} & U_{34} & U_{37} & U_{38} \\ U_{43} & U_{44} & U_{47} & U_{48} \\ U_{73} & U_{74} & U_{77} & U_{78} \\ U_{83} & U_{84} & U_{87} & U_{88} \end{bmatrix} \begin{Bmatrix} M_y \\ -V_x \\ M_x \\ V_y \end{Bmatrix}_{SU} + \begin{Bmatrix} U_{39} \\ U_{49} \\ U_{79} \\ U_{89} \end{Bmatrix} = \begin{Bmatrix} 0 \\ 0 \\ 0 \\ 0 \end{Bmatrix}_{FE} \tag{8}$$

$$\begin{bmatrix} U_{13} & U_{14} & U_{17} & U_{18} \\ U_{23} & U_{24} & U_{27} & U_{28} \\ U_{53} & U_{54} & U_{57} & U_{58} \\ U_{63} & U_{64} & U_{67} & U_{68} \end{bmatrix} \begin{Bmatrix} M_y \\ -V_x \\ M_x \\ V_y \end{Bmatrix}_{SU} = \begin{Bmatrix} u_x \\ \theta_y \\ -u_y \\ \theta_x \end{Bmatrix}_{FE} \tag{9}$$

where *SU* designates the state vector at the support and *FE* designates the state vector at the free end. The procedure for obtaining the forced response is discussed in detail in Part I [1]. Transformation into an inertial reference frame results in the magnitude of the total tilt γ of the rotor, which when neglecting constant offset is found to be

$$\gamma = \frac{1}{2}[(\theta_{x_r} + i\theta_{x_i} + i\theta_{y_r} - \theta_{y_i})e^{i2nt}] \tag{10}$$

where the subscripts r and i denote real and imaginary response components, and t represents time. The appearance of a 2X harmonic response component of the tilt is immediately evident; the magnitude of this component is $\frac{1}{2}|\theta_{x_r} + i\theta_{x_i} + i\theta_{y_r} - \theta_{y_i}|$.

The procedure outlined above provides the ability to include both the localization of the crack and the crack depth. The crack model presented above is accurate for cracks obeying several criteria. First, the crack must terminate in a sharp tip along the length b of the crack edge [23]. Also, the crack must remain open and have a negligible width [4,24]. Finally, the crack flexibility coefficients calculated in Eq. (2) are valid only for cracks up to 80% depth [3].

3 Forced Response: Notched Crack Model

As stated above, the SERR approach is valid only for narrow cracks terminating in a sharp tip. However, for experimental purposes, it is easier to manufacture a finite-width notch than to subject the shaft to lengthy fatigue testing to generate a crack. In addition, the width and depth of a crack manufactured as a notch

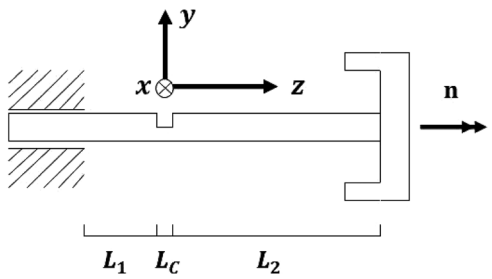

Fig. 3 Cross section of shaft containing transverse notch crack

are easier to measure and quantify than the width and depth of a crack generated through prolonged fatigue testing.

An overhung rotordynamic system displaying an exaggerated notch crack is shown in Fig. 3. As before, the *xyz* frame shown in the figure is a shaft fixed reference frame that rotates with the shaft. The width of the notch is L_c, the length of the beam to the left of the notch is L_1, and the length of the beam to the right of the notch is L_2. The cross section of the shaft follows the designation provided in Fig. 1.

A notch crack transfer matrix model is derived by following the procedure dictated by Lee and Green [14] for generating a general field matrix. A shaft-fixed centroidal set of axes $\bar{x}\bar{y}$ is defined parallel to the *xy* frame shown in Fig. 1, though attached to the centroid of the cracked cross-section. The asymmetric field matrix for a system of centroidal area moments of inertia $I_{\bar{x}}$ and $I_{\bar{y}}$ is

$$[F_{\text{notch}}] = \begin{bmatrix} [F_X]_{4\times4} & [0]_{4\times4} & 0 \\ [0]_{4\times4} & [F_Y]_{4\times4} & 0 \\ 0 & 0 & 1 \end{bmatrix}_{9\times9} \tag{11}$$

where

$$[F_X]_{4\times4} = \begin{bmatrix} 1 & L_c & \frac{L_c^2}{2EI_{\bar{y}}} & \frac{L_c^3}{6EI_{\bar{y}}} \\ 0 & 1 & \frac{L_c}{EI_{\bar{y}}} & \frac{L_c^2}{2EI_{\bar{y}}} \\ 0 & 0 & 1 & L_c \\ 0 & 0 & 0 & 1 \end{bmatrix}_{4\times4} \tag{12}$$

and

$$[F_Y]_{4\times4} = \begin{bmatrix} 1 & L_c & \frac{L_c^2}{2EI_{\bar{x}}} & \frac{L_c^3}{6EI_{\bar{x}}} \\ 0 & 1 & \frac{L_c}{EI_{\bar{x}}} & \frac{L_c^2}{2EI_{\bar{x}}} \\ 0 & 0 & 1 & L_c \\ 0 & 0 & 0 & 1 \end{bmatrix}_{4\times4} \tag{13}$$

The width of the notch beam element is L_c and the elastic modulus is E. The centroidal area moments of inertia $I_{\bar{x}}$ and $I_{\bar{y}}$ for the cracked circular cross section shown in Fig. 1 are provided in Appendix B.

As per the discussion on the local flexibility crack model, the overall transfer matrix $[U]$ is found through successive multiplication of elemental transfer matrices:

$$[U] = [P][F_2][F_{\text{notch}}][F_1] \tag{14}$$

The magnitude of the forced response of the rotor tilt is obtained in a manner identical to that shown in Eqs. (8)–(10).

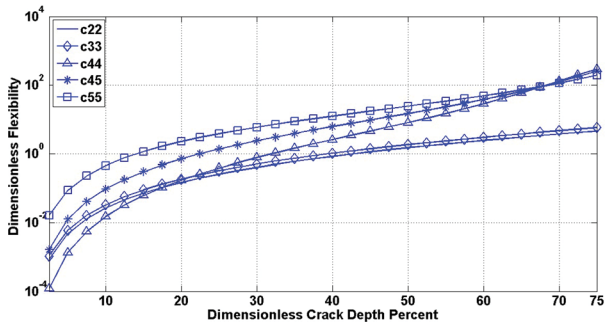

Fig. 4 Dimensionless crack flexibility

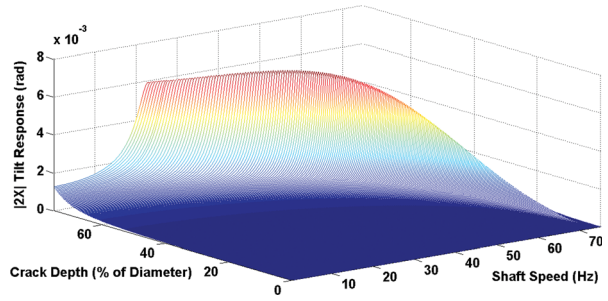

Fig. 5 Local crack flexibility model: magnitude of 2X tilt response

4 Analytic Results: A Comparison Between the Local Crack Flexibility Model and the Notch Model

The degree to which the crack model emulates the real cracked system at hand is crucial towards predicting quantitative characteristics of the response. Perhaps most importantly, a suitable judgment must be made as to what degree the particular cracked system under consideration displays breathing behavior. It is emphasized that the aforementioned models are only valid for a gaping crack.

As stated previously, it is shown in Part I [1] that as crack depth increases the magnitude of the 2X harmonic response at resonance increases, while the frequency at which resonance occurs decreases. The degree to which these phenomena are observed in a cracked system will be investigated using the aforementioned models for cracks of varying depth.

4.1 Local Crack Flexibility Model. The first step in the analysis is to determine the crack flexibility coefficients given by Eq. (3). Dimensionless flexibilities for cracks up to 75% of the diameter are shown in Fig. 4. As expected, the flexibility induced by the crack increases as the crack depth increases.

The parameters for the analysis are provided later in the description of the test rig and the manufactured shaft. The length of the shaft is decreased by approximately 3% such that the 0% crack depth response for both models matches that observed experimentally. The elastic modulus and Poisson ratio are taken to be $207(10)^9$ Pa and 0.33, respectively.

As per Eqs. (8) and (9), the magnitude of the 2X harmonic response of the rotor tilt is plotted in Fig. 5 versus shaft speed and crack depth. A two-dimensional view of Fig. 5 is provided in Fig. 6 for qualitative discussion; darker shades correspond to a larger response magnitude. The frequency at which the 2X harmonic tilt response reaches resonance is plotted along with the 2X tilt resonance magnitude in Fig. 7. As the crack becomes deeper, the shaft speed at which the 2X response reaches resonance diminishes, while the magnitude of the maximum tilt increases (see Figs. 5–7).

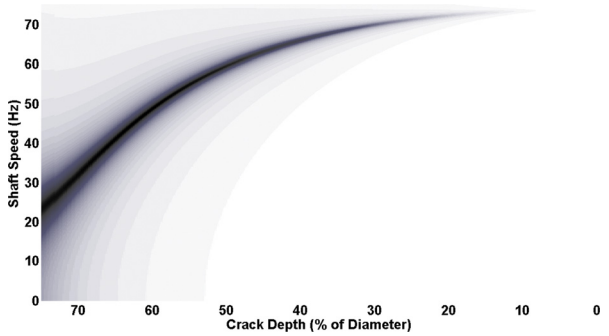

Fig. 6 Local crack flexibility model: magnitude of 2X tilt response versus shaft speed and crack depth

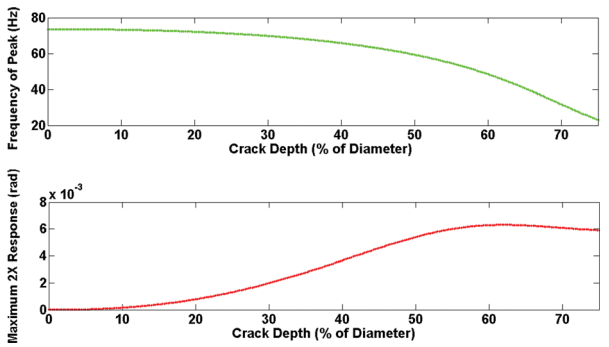

Fig. 7 Local crack flexibility model: magnitude and frequency of 2X tilt resonance

Table 1 2X resonant shaft speeds

	Shaft speed (Hz):c		
% Crack depth	Local crack	Notch crack	Exp.
0	73.56	73.56	73.56
10	73.28	73.45	73.50
20	72.12	73.18	72.92
30	69.80	72.70	71.67
40	65.83	71.81	70.09
50	59.29	70.07	—
60	48.42	66.37	—
70	31.68	57.91	—
75	22.96	50.30	—

The shaft speed at which the 2X harmonic tilt response reaches resonance is one half of a system natural frequency. As the frequency of shaft rotation deviates from this value, the 2X harmonic tilt response magnitude becomes markedly diminished.

It is clear from the second column of Table 1 that from 0% crack depth to 40% crack depth, the frequency of the 2X harmonic tilt resonance diminishes by approximately 11%. However, from 0% crack depth to 60% crack depth, the frequency of the 2X harmonic tilt resonance diminishes by approximately 31%. It is clear that as the crack grows beyond 40% of the shaft diameter, the frequency of the 2X harmonic resonance decreases substantially, accompanied by a substantial increase in magnitude, as seen in Fig. 7.

4.2 Notch Crack Model. The response due to a notch crack is intrinsically tied to the area moments of inertia about different axes. As the ratio of the area moments of inertia increases, the magnitude of the 2X harmonic response is predicted to increase.

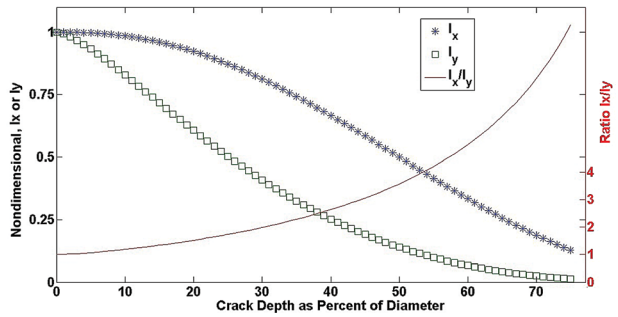

Fig. 8 Notch area moments of inertia

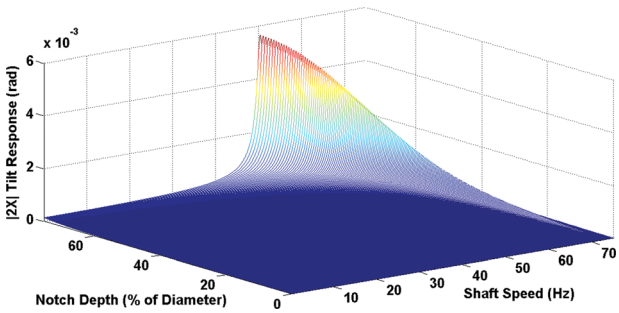

Fig. 9 Notch crack model: magnitude of 2X tilt response

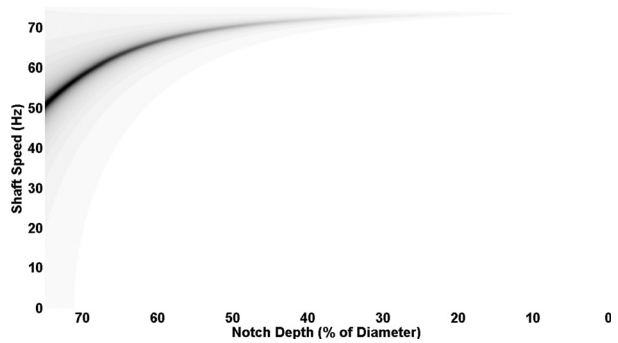

Fig. 10 Notch crack model: 2X tilt response versus shaft speed and crack depth

To assist in interpretation of the results, nondimensional area moments of inertia for a cracked circular cross section are shown in Fig. 8, generated using the relations provided in Appendix B. It is clear from the figure that as notch crack depth increases, the ratio of the centroidal area moments of inertia likewise increases: It is, therefore, expected that the response magnitude increases as notch depth increases.

The magnitude of the 2X harmonic response of the rotor tilt is plotted in Fig. 9 versus shaft speed and notch crack depth. A two-dimensional view of Fig. 9 is provided in Fig. 10 where, once again, darker shades correspond to a higher response magnitude. The frequency at which the 2X harmonic tilt reaches resonance is plotted along with the magnitude of the resonant response in Fig. 11. As the notch crack becomes deeper, the shaft speed at which the 2X harmonic response reaches resonance diminishes, while the magnitude of the resonant peak increases (see Figs. 9–11]. Compared to the local crack flexibility model, however, the rate at which the 2X resonance frequency drops as depth increases is much less pronounced.

The 2X resonance frequencies for notch cracks between 0% and 75% depth are provided in Table 1. It is clear from the table that from 0 to 40% depth (maximum depth used in experiments,

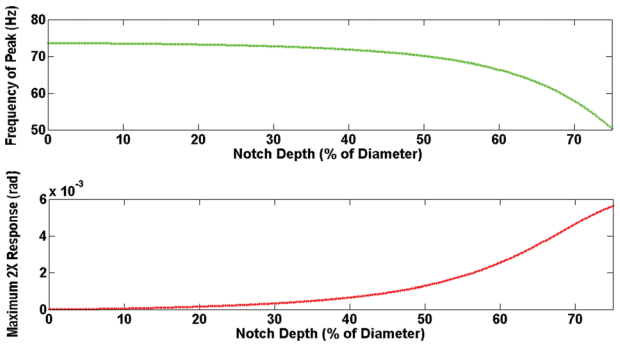

Fig. 11 Notch crack model: magnitude and frequency of 2X harmonic tilt resonance

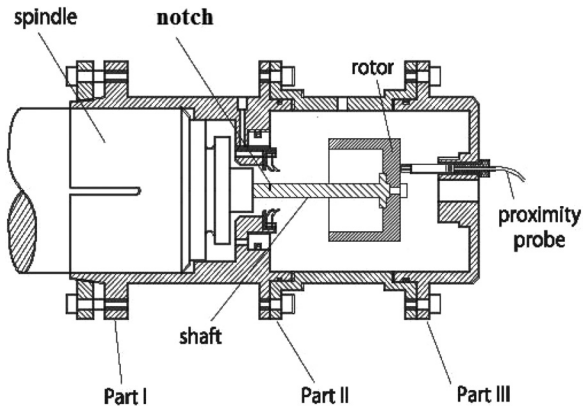

Fig. 12 Test rig cross section

for safety reasons), the 2X resonance frequency decreases by only 2.4%. However, from 0 to 60% depth the 2X resonance frequency decreases by approximately 9.8%.

5 Experimental Test Rig

The objective of the experimental work is to investigate the feasibility of using the 2X harmonic tilt response component to detect a crack in an existing FMR mechanical face seal contact monitoring system.

Higher harmonics are present in the frequency spectrum of most real rotor dynamic systems. These harmonics can be attributed to characteristics such as asymmetric bearings, rubbing contact within the system, and general nonlinear behavior [7,20,25]. For this reason, the mere presence of a higher harmonic does not indicate a particular fault. As such, further signatures must be employed to distinguish faults.

5.1 Test Rig Overview. Though only a concise description is given here, a comprehensive description of the test rig used to detect seal face contact is found in [14,23]. The cross section of the test rig is shown in Fig. 12. The test rig consists of a precision spindle into which a shaft is screwed. The three part housing assembly is labeled "Part I," "Part II," and "Part III." The spindle is driven by a dc motor with a maximum speed of 1750 rpm. A 1:4 gear ratio of the motor to the spindle provides a maximum spindle rotation speed of 7000 rpm.

Gaping cracks varying from 0% to 40% of the shaft diameter are manufactured in the shaft 6.35 mm from the base using electrical discharge machining (EDM). It is important to note that the EDM process can create corners within the notch that are not exactly rectangular but instead have a finite corner radius. The effect of this radius is assumed to be small, however, and the

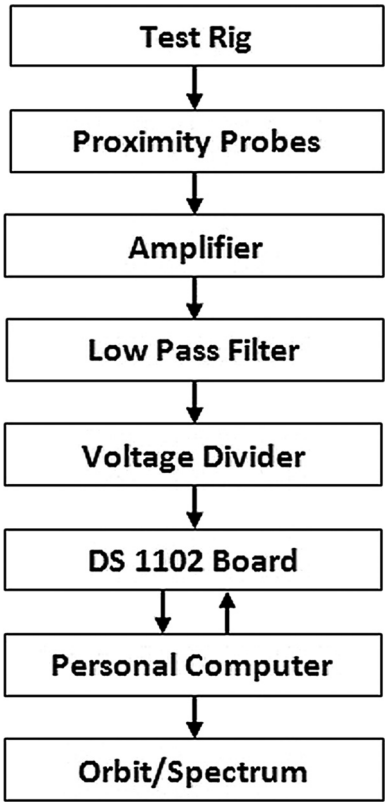

Fig. 13 Monitoring system block diagram

corners assumed to be sharp. The width of the crack is approximately 1.0 mm. The manufactured rectangular shape of the crack indicates that the crack is perhaps best modeled using a notch crack model, such as that discussed above.

The shaft is composed of AISI 4140 steel of diameter 10.16 mm and length 88.9 mm. The rotor has a mass of 0.5733 kg, polar mass moment of inertia of $3.847(10)^{-4}$ kg · m^2 and a transverse mass moment of inertia of $2.371(10)^{-4}$ kg · m^2. The center of gravity of the rotor is axially offset from the end of the shaft by a distance of 10.4 mm. The surface of the rotor is polished to a surface roughness of 0.1 μm (rms) to provide accurate probe data readings.

5.2 Monitoring System. A block diagram schematic of the monitoring system is shown in Fig. 13. The dynamic response of the rotor is measured via three eddy-current proximity probes (one of which is shown in Fig. 12). The probes produce a voltage proportional to the distance from the end of the probe to the surface of the rotor. The bandwidth of the probes is approximately 10 kHz, and the signal from the probes is first passed through a 1 kHz low-pass filter to prevent high frequency cross-talk and aliasing. Following the low-pass filter, the signal passes through a voltage divider that drops the voltage from -21.2 V to -10 V, which is required for input to the control board. The control board is a dSPACE DS1102 floating-point controller board with both analog-to-digital and digital-to-analog conversion, as well as fully programmable processing capabilities [23].

The probe layout used to measured seal face contact is provided in Ref. [23]. The orientation of the probes is adjusted to best observe the gravity induced tilt about the η axis: an optimum layout places probes a maximum distance from the η axis. The probe layout is shown in Fig. 14 about an inertial η ξ frame that does not rotate with the shaft. Gravity acts in the ξ direction, as shown in the figure. Probe C is inclined 60 deg above the η axis, and probes A and B are rotated 90 deg and 180 deg counterclockwise from this position, respectively.

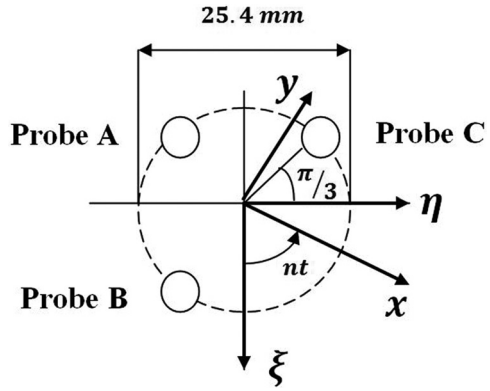

Fig. 14 Adapted probe configuration

The probes are capable of measuring tilts γ_η and γ_ξ about each axis. The rotating reference frame xy used in the analytic development is shown in the figure to provide reference. A plot of γ_η versus γ_ξ provides the angular response orbit of the rotor.

5.3 Shaft Damping. A frequency-independent structural damping model is used to incorporate energy dissipation. Viscous damping constants equivalent to the structurally damped system are incorporated into the point matrix provided by Casey and Green [1] (the point matrix is summarized in Appendix A). The energy dissipated per cycle via viscous damping is

$$E_{\text{dis}_v} = \pi\omega c|X|^2 \tag{15}$$

while the energy dissipated via structural damping per cycle is

$$E_{\text{dis}_s} = \pi\beta k|X|^2 \tag{16}$$

where ω is the response frequency, c is the equivalent viscous damping coefficient, k is the stiffness, β is the structural damping constant, and $|X|$ is the magnitude of the response. A value for an equivalent viscous damping coefficient c_{eq} is obtained by relating Eqs. (15) and (16) and solving for c (which is now the equivalent viscous damping coefficient c_{eq}):

$$c_{eq} = \frac{\beta k}{\omega} \tag{17}$$

An accelerometer is placed on the end of the nonrotating shaft and the system is set into oscillatory motion; the output from the accelerometer is used to measure the response of the system. A log-decrement approach is used, in conjunction with Eq. (17), to provide an estimate for β of 0.00981. Appendix A discusses the relationship between β and the damping coefficients d_{ij} appearing in the equations of motion.

Several assumptions are made in the development of the damping model. Though structural damping has been shown to occur independent of frequency over a wide frequency range, there is still significant difference between the frequency of response at which the damping experiments are conducted (700 Hz) and the frequency at which crack detection experiments are conducted (60–150 Hz). Also, the stiffness was approximated using the globally asymmetric shaft model as a worst-case scenario. It is assumed that the crack does not introduce additional damping into the system.

6 Experimental Results

Experimental results for manufactured shaft notch cracks up to 40% depth are provided for comparison against analytic results (though analytic results are given for crack depths up to 75%, the experiments were only carried out to 40% crack depth for safety

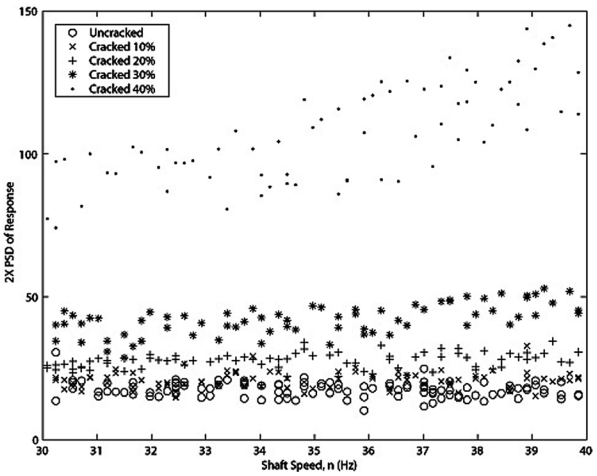

Fig. 15 Low speed range of experimental 2X response

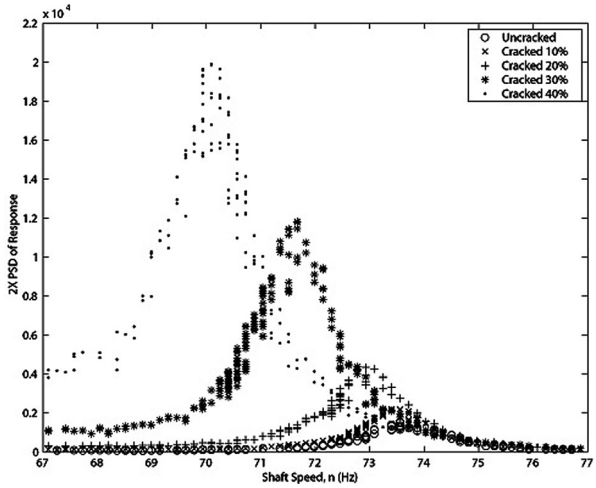

Fig. 16 High speed range of experimental 2X response

reasons). It is shown analytically that the 2X harmonic response is maximum at shaft speeds equal to one-half of a natural frequency. An increase in the depth of the crack causes the natural frequencies to decrease (as seen by a decreased 2X resonance frequency) while the amplitude of the resonance increases.

6.1 2X Tilt Response Results. The following procedure is employed to generate experimental plots of the magnitude of the 2X tilt response component as a function of shaft speed. The shaft speed is incrementally adjusted, and a time sample of the probe data is taken by the DS1102 board. The power spectral density (PSD) of the time data is computed, and the 2X harmonic response magnitudes of the tilt are obtained via filtering of the total signal. The process is repeated for cracks varying between 0% and 40% depth. A single shaft specimen is utilized in the experiments, and the crack depth is incrementally adjusted for each subsequent set of experiments. A single shaft is used in order to mitigate potential variations in a set of shaft specimens and to isolate the effect of crack depth on the system response.

Figures 15 and 16 show the scaled 2X PSD amplitude of the response provided by one of the probes as a function of shaft speed for the low and high shaft speed ranges, respectively. The experimentally observed 2X resonance frequencies are extracted and provided in the last column of Table 1. As the crack increases from 0% depth to 40% depth, the frequency of the 2X resonant peak decreases by approximately 4.7%.

Recall that from 0 to 40% crack depth, the local crack flexibility model predicted an 11% decrease in the 2X resonant peak frequency while the notch model predicted a 2.4% decrease. It is clear that the experimentally measured decrease of 4.7% lies between the analytically predicted values. A plausible conjecture for this result is that the manufactured notched crack was neither purely a local crack nor purely a stiffness asymmetry (the notch model includes only stiffness asymmetry to approximate the crack). It is likely that the actual manufactured crack includes characteristics of both models. The finite-width nature of the crack creates a corresponding stiffness asymmetry similar to the notch model, while stress concentrations due to the sharp edges contained within the crack incorporate aspects of the local crack flexibility model (recall that the local crack flexibility model is developed using stress concentration factors). Additionally, the discrepancy between the experimental results and the notch crack results could be caused by neglecting the inertia of the shaft when compared to the rotor.

6.2 Tilt Orbit Monitoring and Orbit Shape. The probe signal is filtered to extract only the 2X component of the angular response orbit caused by the crack. Since the seal has been removed in these experiments, the measured 2X harmonic response component is solely due to the crack.

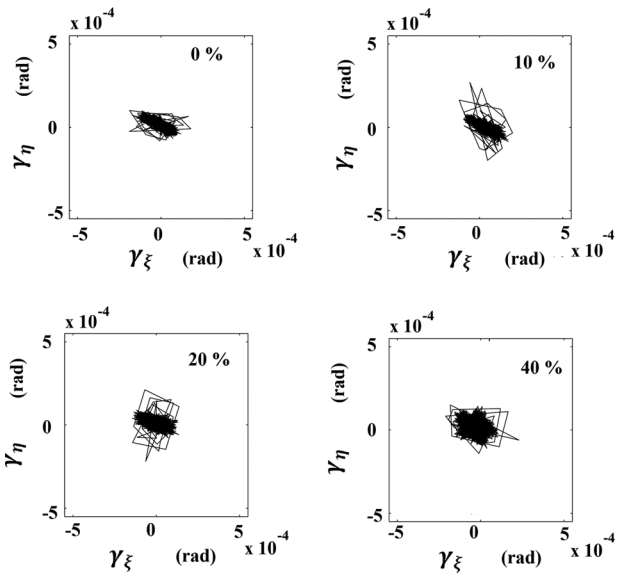

Fig. 17 Experimental 2X content of tilt orbit: 40 Hz

Figure 17 shows the 2X content of the angular response orbit for a 40 Hz shaft speed (within the low frequency regime) that does not contain 2X resonance; γ_η and γ_ξ are the prior discussed tilts about the η and ξ axes, respectively. The depth of the crack is indicated in the plot. It is clear that the magnitude of the 2X angular response orbit increases slightly as crack depth increases. The shape of the orbit displays some elliptical behavior.

The elliptical behavior of the 2X component of the angular response orbit becomes much more pronounced for larger cracks near resonance, as seen in Fig. 18 for a 71 Hz shaft speed. It is clear from the plot that the 2X component of the angular response orbit occurs predominantly about the η direction since the rotation caused by gravity is primarily about this axis. Similar plots for a wide range of frequencies are provided in Ref. [23].

Since this work focuses on exploring the feasibility of using an existing monitoring system to detect an additional system fault, it is important to consider conflicts arising due to the presence of both faults simultaneously. The seal face contact detection system diagnoses contact based on relative variance between the proximity probe signals [21,26–28]. However, the total tilt orbit shape

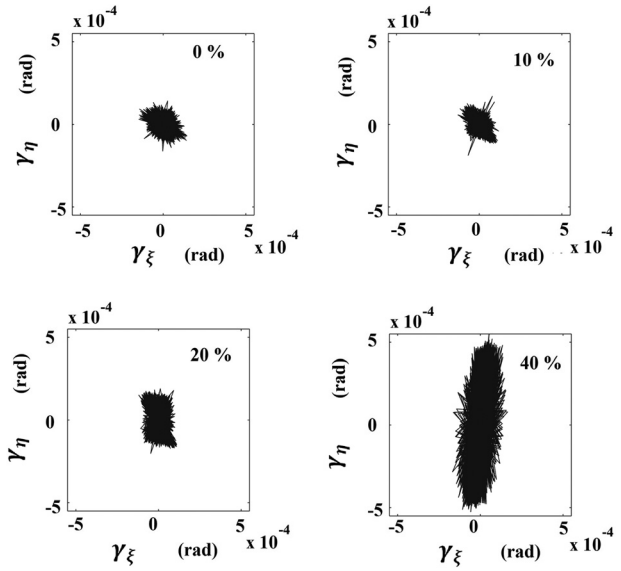

Fig. 18 Experimental 2X content of tilt orbit: 71 Hz

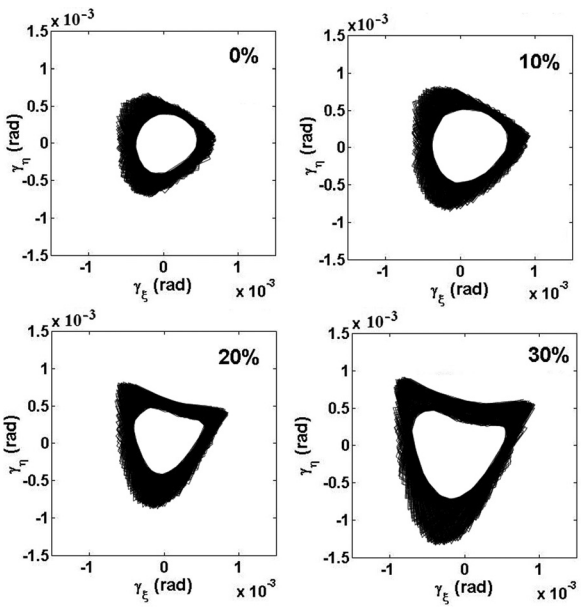

Fig. 19 Experimental total tilt orbits near respective 2X resonance locations for cracks between 0% and 30% depth

for the sealing system when contact is occurring is mostly circular [28]. For a cracked shaft, the total tilt orbit shape is decidedly asymmetric, as shown in Figs. 19 and 20. Evident from Figs. 19 and 20 is the observation that as crack depth increases, the asymmetric nature of the total angular response orbit increases, with important implications for simultaneous multiple fault detection.

6.3 Feasibility of Simultaneous Multiple Fault Detection. Lee and Green [20] show that higher harmonics, including the 2X harmonic, are influenced by seal face contact. To simultaneously detect seal face contact and transverse shaft cracks, significantly different response characteristics must be demonstrated for each fault. It is observed that the magnitude of the 2X harmonic induced by a transverse shaft crack decreases substantially when the shaft speed is far from the 2X resonance frequency.

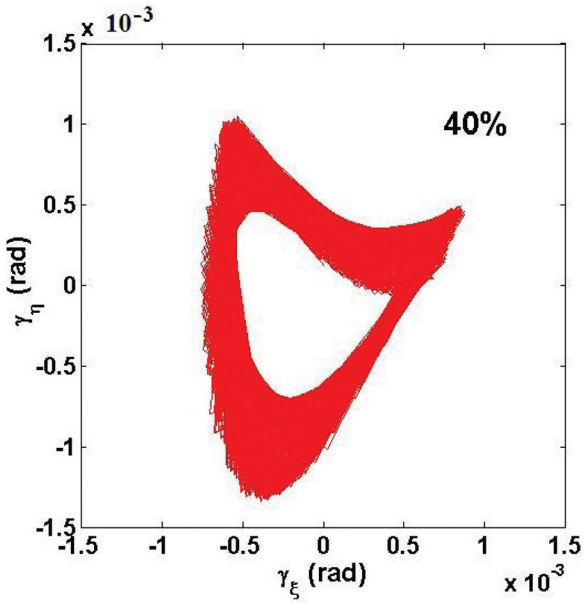

Fig. 20 Experimental total tilt orbit near 2X resonance for 40% crack depth

Seal face contact, however, results in the appearance of integer harmonics for many shaft speeds [20]. In addition, observation of the total tilt orbit shape could distinguish the faults, as the total tilt orbit shape is highly asymmetric for a large transverse shaft crack while mostly circular for seal face contact. For small cracks (up to 20%) with only a slight amount of asymmetry in the total angular response orbit, higher harmonics (3X, 4X, etc.) can be employed to distinguish the faults. The difference in these signatures suggests that it is plausible that the monitoring system developed for seal face contact can be successfully adapted to simultaneously detect vastly different types of faults.

7 Conclusions

It is clear that the model selected to approximate the crack is imperative towards quantitatively predicting response characteristics. The 2X resonant frequency of the tilt estimated by the local crack flexibility model decreases at a decidedly higher rate than that predicted by the notch crack model. However, the experimental results are observed to decrease at a rate that is between those predicted by the local crack flexibility model and the notch crack model. It is likely that the decrease is indicative of a hybrid crack model displaying characteristics of both models. The finite width and rectangular geometry of the crack indicate a notch crack model, while the stress concentrations within the notch introduce additional compliances similar to the local crack flexibility model.

A test rig designed for mechanical face seal contact is modified to detect the presence of a transverse shaft fatigue crack. Experimental results of the magnitude of the 2X harmonic tilt response are provided for cracks between 0% and 40% depth. In addition, the 2X component of the angular response orbit is extracted and plotted for two shaft speed regimes: one far from the 2X resonant frequency and one near the 2X resonance frequency. As the shaft speed draws closer to the 2X resonance frequency and the crack depth increases, the elliptical nature of the 2X component of the angular response orbit becomes more pronounced.

The feasibility of using the existing system to simultaneously detect transverse shaft cracks and seal face contact is discussed. While both gaping shaft cracks and seal face contact induce a 2X harmonic response component, significant differences exist

between the response profiles. First, seal face contact induces shaft speed harmonics for many integers of the shaft speed. Secondly, the total angular response orbit for seal face contact is mostly circular, whereas the total angular response orbit for a system displaying a shaft crack is highly asymmetric. Therefore, it is concluded that the existing vibration monitoring system is indeed capable of distinguishing shaft cracks and seal face contact.

Acknowledgment

This material is based upon work supported by the National Science Foundation under Grant No. 1100101.

Nomenclature

E = elastic modulus
I_i = area moment of inertia about the i^{th} axis
L = length of field element
M = bending moment
P_i = force in i^{th} direction
V = shear force
X = magnitude of response
$[C]$ = crack compliance matrix
$[F]$ = field matrix
$[P]$ = point matrix
$[U]$ = overall transfer matrix
$\{S\}$ = transfer matrix state vector
a = crack depth
b = length of half of crack edge
c_{eq} = equivalent viscous damping coefficient
c_{ij} = compliance in i^{th} direction by force in j^{th} direction
n = shaft speed
u = linear deflection
u_i = displacement in i^{th} direction
β = structural damping coefficient
γ = magnitude of rotor tilt
θ = angular deflection
ν = Poisson ratio
ω = frequency of response
r, i = real/imaginary response component
x, y = direction of state vector terms

Appendix A: Transfer Matrices

Lee and Green [14] provide the general 9×9 field matrix for beam segment i undergoing two-plane bending:

$$[F]_i = \begin{bmatrix} 1 & L & \frac{L^2}{2EI} & \frac{L^3}{6EI} & 0 & 0 & 0 & 0 & 0 \\ 0 & 1 & \frac{L}{EI} & \frac{L^2}{2EI} & 0 & 0 & 0 & 0 & 0 \\ 0 & 0 & 1 & L & 0 & 0 & 0 & 0 & 0 \\ 0 & 0 & 0 & 1 & 0 & 0 & 0 & 0 & 0 \\ 0 & 0 & 0 & 0 & 1 & L & \frac{L^2}{2EI} & \frac{L^3}{6EI} & 0 \\ 0 & 0 & 0 & 0 & 0 & 1 & \frac{L}{EI} & \frac{L^2}{2EI} & 0 \\ 0 & 0 & 0 & 0 & 0 & 0 & 1 & L & 0 \\ 0 & 0 & 0 & 0 & 0 & 0 & 0 & 1 & 0 \\ 0 & 0 & 0 & 0 & 0 & 0 & 0 & 0 & 1 \end{bmatrix}_{9\times 9} \tag{A1}$$

The compliance matrix (see Eq. (3)) is rearranged to provide the crack flexibility transfer matrix, $[F_{\text{crack}}]$ (note the expansion from 8×8 to 9×9):

$$[F_{\text{crack}}] = \begin{bmatrix} 1 & 0 & 0 & -c_{22} & 0 & 0 & 0 & 0 & 0 \\ 0 & 1 & c_{44} & 0 & 0 & 0 & c_{45} & 0 & 0 \\ 0 & 0 & 1 & 0 & 0 & 0 & 0 & 0 & 0 \\ 0 & 0 & 0 & 1 & 0 & 0 & 0 & 0 & 0 \\ 0 & 0 & 0 & 0 & 1 & 0 & 0 & -c_{33} & 0 \\ 0 & 0 & c_{54} & 0 & 0 & 1 & c_{55} & 0 & 0 \\ 0 & 0 & 0 & 0 & 0 & 0 & 1 & 0 & 0 \\ 0 & 0 & 0 & 0 & 0 & 0 & 0 & 1 & 0 \\ 0 & 0 & 0 & 0 & 0 & 0 & 0 & 0 & 1 \end{bmatrix}_{9\times 9} \tag{A2}$$

The point matrix, developed in the rotating reference frame xy shown in Fig. 1, is

$$[P] = \begin{bmatrix} [D]_{4\times 4} & -[G]_{4\times 4} & 0 \\ [G]_{4\times 4} & [D]_{4\times 4} & 0 \\ 0 & 0 & 1 \end{bmatrix}_{9\times 9} \tag{A3}$$

where

$$[D] = \begin{bmatrix} 1 & 0 & 0 & 0 \\ 0 & 1 & 0 & 0 \\ 0 & (I_p - I_t)n^2 - I_t p_r^2 & 1 & 0 \\ m(p_r^2 + n^2) & 0 & 0 & 1 \end{bmatrix}_{4\times 4} \tag{A4}$$

and

$$[G] = \begin{bmatrix} 0 & 0 & 0 & 0 \\ 0 & 0 & 0 & 0 \\ 0 & -i(2I_t - I_p)np_r & 0 & 0 \\ 2imnp_r & 0 & 0 & 0 \end{bmatrix}_{4\times 4} \tag{A5}$$

The mass of the lumped inertia is m, the transverse and polar mass moments of inertia are I_t and I_p, respectively; n is the shaft speed; and p_r is the relative whirl speed (for a gravity-forced response analysis, $p_r = n$). Damping and forcing can be accounted for through the following:

$$[P_{\text{tot}}] = [P] + [P'] \tag{A6}$$

where

$$[P'] = \begin{bmatrix} 0 & 0 & 0 & 0 & 0 & 0 & 0 & 0 & 0 \\ 0 & 0 & 0 & 0 & 0 & 0 & 0 & 0 & 0 \\ ind_{12_Y} & -ind_{22_Y} & 0 & 0 & 0 & 0 & 0 & 0 & 0 \\ ind_{11_Y} & -ind_{12_Y} & 0 & 0 & 0 & 0 & 0 & 0 & mg \\ 0 & 0 & 0 & 0 & 0 & 0 & 0 & 0 & 0 \\ 0 & 0 & 0 & 0 & 0 & 0 & 0 & 0 & 0 \\ 0 & 0 & 0 & 0 & ind_{12_X} & -ind_{22_X} & 0 & 0 & 0 \\ 0 & 0 & 0 & 0 & ind_{11_X} & -ind_{12_X} & 0 & 0 & -img \\ 0 & 0 & 0 & 0 & 0 & 0 & 0 & 0 & 0 \end{bmatrix}_{9\times 9} \tag{A7}$$

The shaft speed is n, g is the acceleration due to gravity, and the damping coefficients d_{ij_q} are equivalent to the $c_{eq_{ij}}$ values provided in Eq. (17). The stiffness value k is taken to be the

average of the stiffness values about the x and y axes, as discussed in Ref. [1].

Appendix B: Area Moments of Inertia

An integral aspect of the notch crack model is calculation of the area moments of inertia about the shaft-fixed centroidal axes $\bar{x}$ and $\bar{y}$, which are parallel to the shaft-fixed axes x and y shown in Fig. 1. Note that the axes x and y are affixed to the shaft at the geometric center of the circular, uncracked cross section.

The area moments of inertia I_x and I_y about the x and y axes shown in Fig. 1 are found to be

$$I_x = \frac{(R-a)b}{4}\left[\frac{2}{3}b^2 + R^2\right] + \frac{\pi R^4}{8} + \frac{R^4}{4}\tan^{-1}\left(\frac{R-a}{b}\right) \tag{B1}$$

$$I_y = \frac{(R-a)b}{4}\left[R^2 - 2b^2\right] + \frac{\pi R^4}{8} + \frac{R^4}{4}\tan^{-1}\left(\frac{R-a}{b}\right) \tag{B2}$$

where b, the length of the crack, is $b = \sqrt{2Ra - a^2}$. However, the area moments of inertia must be found about the centroid of the cracked cross section rather than the centroid of the intact cross section. The parallel axis theorem is, therefore, employed (note that the x and $\bar{x}$ axes coincide) to find the centroidal area moments of inertia $I_{\bar{x}}$ and $I_{\bar{y}}$:

$$I_{\bar{x}} = I_x \tag{B3}$$

$$I_{\bar{y}} = I_y - A\bar{y}^2 \tag{B4}$$

where $\bar{x}$ is the distance along y between the centroid and the center of the intact cross section, given by Casey and Green [1] to be

$$\bar{x} = \frac{2}{3A}b^3 \tag{B5}$$

The area A is found to be

$$A = (R-a)b + R^2\sin^{-1}\left(1 - \frac{a}{R}\right) + \frac{\pi R^2}{2} \tag{B6}$$

The resulting area moments of inertia are made nondimensional by dividing by the respective area moment of inertia of the intact cross section. The nondimensional area moments of inertia are then normalized to a value of one for 0% crack depth.

References

[1] Green, I., and Casey, C., 2005, "Crack Detection in a Rotor Dynamic System by Vibration Monitoring—Part I: Analysis," ASME J. Engr. Gas Turb. Power, **127**(2), pp. 425–436.

[2] Rao, J. S., 1996, *Rotor Dynamics*, 3rd ed. New Age International, New Delhi.

[3] Papadopoulos, C. A., and Dimarogonas, A. D., 1987, "Coupled Longitudinal and Bending Vibrations of a Rotating Shaft With an Open Crack," J. Sound Vib., **117**(1), pp. 81–93.

[4] Papadopoulos, C., 2008, "The Strain Energy Release Approach for Modeling Cracks in Rotors: A State of the Art Review," Mech. Syst. Signal Process., **22**(4), pp. 763–789.

[5] Mayes, I., and Davies, W., 1976, "The Vibrational Behaviour of a Rotating Shaft System Containing a Transverse Crack," Proceedings of the Institution of Mechanical Engineers, Conference on Vibrations in Rotating Machinery, London, pp. 53–64.

[6] Grabowski, B., 1980, "The Vibrational Behavior of a Turbine Rotor Containing a Transverse Crack," J. Mech. Des. Trans. ASME, **102**, pp. 140–146.

[7] Imam, I., Azzaro, S., Bankert, R. J., and Scheibel, J., 1989. "Development of an Online Rotor Crack Detection and Monitoring System," J. Vib. Acoust. Stress, **111**, pp. 241–250.

[8] Gasch, R., 1976, "Dynamic Behavior of a Simple Rotor With a Cross-Sectional Crack," Proceedings of the Institution of Mechanical Engineers, Conference on Vibrations in Rotating Machinery, London, pp. 123–128.

[9] Dimarogonas, A., and Papadopoulos, C., 1983, "Vibration of Cracked Shafts in Bending," J. Sound Vib., **91**(4), pp. 583–593.

[10] Darpe, A., Gupta, K., and Chawla, A., 2004, "Coupled Bending, Longitudinal and Torsional Vibrations of a Cracked Rotor," J. Sound Vib., **269**(1), pp. 33–60.

[11] Gounaris, G., and Papadopoulos, C., 2002. "Crack Identification in Rotating Shafts by Coupled Response Measurements," Eng. Fract. Mech., **69**(3), pp. 339–352.

[12] Wauer, J., 1990, "Modeling and Formulation of Equations of Motion for Cracked Rotating Shafts," Int. J. Solid. Struct., *26*(8), pp. 901–914.

[13] Dimarogonas, A., and Paipetis, S., 1983, *Analytical Methods in Rotor Dynamics*. Applied Science Publishers, London.

[14] Lee, A., and Green, I., 1994, "Rotordynamics of a Mechanical Face Seal Riding on a Flexible Shaft," ASME J. Tribol., **116**(2), pp. 345–351.

[15] Pestel, E., and Leckie, F., 1963, *Matrix Methods in Elastomechanics*, McGraw-Hill, New York.

[16] Gasch, R., 1993, "A Survey of the Dynamic Behaviour of a Simple Rotating Shaft With a Transverse Crack," J. Sound Vib., **160**(2), pp. 313–332.

[17] Wauer, J., 1990, "On the Dynamics of Cracked Rotors: A Literature Survey," Appl. Mech. Rev., **43**(1), pp. 13–17.

[18] Lee, A., and Green, I., 1995, "Physical Modeling and Data Analysis of the Dynamic Response of a Flexibly Mounted Rotor Mechanical Seal," ASME J. Tribol., **117**, pp. 130–135.

[19] Lee, A., and Green, I., 1995. "An Experimental Investigation of the Steady-State Response of a Noncontacting Flexibly Mounted Rotor Mechanical Face Seal," ASME J. Tribol., **117**, pp. 153–159.

[20] Lee, A., and Green, I., 1994, "Higher Harmonic Oscillations in a Non-contacting FMR Mechanical Face Seal Test Rig," J. Vib. Acoust. Trans. ASME, **116**(2), pp. 161–167.

[21] Dayan, J., Zou, M., and Green, I., 2002, "Contact Elimination in Mechanical Face Seals Using Active Control," IEEE T. Contr. Syst. T., **10**(3), pp. 344–354.

[22] Irwin, G., 1957, "Analysis of Stresses and Strains Near the End of a Crack Traversing a Plate," ASME J. Appl. Mech., **24**, pp. 361–364.

[23] Casey, C., 2000, "Crack Detection in a Rotordynamic System by Vibration Monitoring," Master's thesis, Georgia Institute of Technology, Atlanta, GA.

[24] Gounaris, G., Papadopoulos, C., and Dimarogonas, A., 1996, "Crack Identification in Beams by Coupled Response Measurements," Comput. Struct., **58**(2), pp. 299–305.

[25] Bently, D., and Muszynska, A., 1986, "Early Detection of Shaft Cracks on Fluid-Handling Machines," Proceedings of ASME International Symposium on Fluid Machinery Trouble Shooting, 1986 Winter Annual Meeting, Anaheim, CA, December 7, pp. 53–58.

[26] Zou, M., Dayan, J., and Green, I., 2000, "Dynamic Simulation and Monitoring of a Non-Contacting Flexibly Mounted Rotor Mechanical Face Seal," P. I. Mech. Eng. C J. Mec., **214**(9), pp. 1195–1206.

[27] Dayan, J., Zou, M., and Green, I., 2000, "Sensitivity Analysis for the Design and Operation of a Non-Contacting Mechanical Face Seal," P. I. Mech. Eng. C J. Mec., **214**(9), pp. 1207–1218.

[28] Zou, M., Dayan, J., and Green, I., 2000, "Feasibility of Contact Elimination of a Mechanical Face Seal Through Clearance Adjustment," ASME J. Eng. Gas Turb. Power, **122**, pp. 478–484.